

NASA/CR-1999-209341  
ICASE Report No. 99-19



## **On the Stability of Three-dimensional Boundary Layers Part 2: Secondary Instability**

*Erik Janke*  
*Old Dominion University, Norfolk, Virginia*

*Ponnampalam Balakumar*  
*Old Dominion University, Norfolk, Virginia*  
*and*  
*ICASE, Hampton, Virginia*

*Institute for Computer Applications in Science and Engineering*  
*NASA Langley Research Center*  
*Hampton, VA*

*Operated by Universities Space Research Association*



National Aeronautics and  
Space Administration

Langley Research Center  
Hampton, Virginia 23681-2199

Prepared for Langley Research Center  
under Contract NAS1-97046

June 1999

# ON THE STABILITY OF THREE-DIMENSIONAL BOUNDARY LAYERS

## PART 2: SECONDARY INSTABILITY \*

ERIK JANKE AND PONNAMPALAM BALAKUMAR

**Abstract.** The secondary instability of three-dimensional incompressible boundary layers is studied using Floquet theory. Starting from the equilibrium solutions that we obtained from the PSE computations documented in Part 1, we investigate the region where a purely stationary crossflow disturbance saturates for its secondary instability characteristics utilizing developed global and local eigenvalue solvers that are based on the Implicitly Restarted Arnoldi Method, and a Newton-Raphson technique, respectively. The main focuses of this study are on the existence of multiple roots in the eigenvalue spectrum that could explain experimental observations of time-dependent occurrences of an explosive growth of traveling disturbances, on the routes by which high-frequency disturbances enter the boundary layer, as well as on gaining more information about threshold amplitudes for the growth of secondary disturbances.

**Key words.** crossflow, Floquet theory, secondary instability, implicitly restarted Arnoldi method

**Subject classification.** Fluid Dynamics

**1. Introduction.** In the present work, secondary instability is defined as the linear instability of a periodic secondary flow. Due to the nonlinear interaction and saturation of primary stationary disturbances, highly inflectional velocity profiles are formed in all coordinate directions as documented in the first part of the present paper. According to Orszag and Patera [16], these inflectional profiles are the origin of this inviscid instability to high-frequency disturbances that is inherently three-dimensional. Once the disturbances reached a certain threshold amplitude, their explosive growth rapidly leads to transition.

Herbert [7] presented results from an investigation of the secondary instability in plane channel flow. Incorporating the shape-assumption and starting from equilibrium solutions, he solved the linearized disturbance equations as an eigenvalue problem using Floquet theory. He found that the three-dimensional secondary disturbances travel at slightly different phase speeds than the primary two-dimensional disturbances. He further determined threshold amplitudes for the onset of different secondary instability modes for primary disturbance amplitudes of less than one percent of the freestream velocity and argued that the threshold amplitude physically represents a minimal vorticity concentration that must overcome the viscous damping of the secondary instabilities. Finally, he pointed out that there is an intricate connection between linear and secondary instability modes that is revealed by considering the limit of a zero amplitude of the primary disturbance.

Reed [14] investigated the existence of a parametric resonance in the region of a finite-amplitude crossflow vortex for flow conditions adapted to the swept flat plate experiment by Saric and Yeates [15]. Using the parallel flow assumption for the mean flow, neglecting the mean flow distortion as well as the amplitude variation in the streamwise direction due to the primary disturbances, and finally superimposing two three-dimensional secondary waves in a moving frame of reference on this flow, she established a Floquet system that was solved using a spectral collocation method. An unstable structure corresponding to the second

---

\*Old Dominion University, Department of Aerospace Engineering, Norfolk, VA 23529 (current emails: [erik.janke@dlr.de](mailto:erik.janke@dlr.de), [pbala@icase.edu](mailto:pbala@icase.edu)). This research was supported by the National Aeronautics and Space Administration under NASA Contract No. NAS1-97046 while the second author was in residence at the Institute for Computer Applications in Science and Engineering (ICASE), NASA Langley Research Center, Hampton, VA 23681.

harmonic of the primary disturbance was found away from the wall, and the results closely reproduced the experimentally observed modification of the dominant wavelength by Saric and Yeates.

From his classical experiment on a swept cylinder, Poll [17] reported occasional instances where high-frequency disturbances were measured on top of the primary disturbances. The frequency of these disturbances was an order-of-magnitude higher than the frequency of the primary disturbances. In the experimental work by Kohama et al. [9] and by Takagi and Itoh [18], it was pointed out that the high-frequency secondary instability originates away from the wall in regions of high vorticity and shear at normal locations of about half the boundary layer thickness. Moreover, Deyhle and Bippes [4] mentioned observations of an explosive growth of traveling modes at the very end of the transition process that looked like a bursting of individual stationary vortices. They also measured a high-frequency disturbance of  $f^*=2.1$  kHz riding on top of the primary waves prior to the local breakdown to turbulence.

Numerical results by Balachandar et al. [1] for rotating-disc flow and by Malik et al. [13] for Swept Hiemenz Flow showed that there are several unstable secondary eigenvalues present in the region of nonlinear saturation, and that the developing instability structures travel on the back of the primary stationary crossflow vortices. Their growth was attributed to combined vortex stretching and tilting in the presence of strong flow gradients. Both for rotating-disc flow as for Swept Hiemenz Flow, the inclination of the secondary instability structures with respect to the constant phase lines was determined between  $40^\circ$ - $50^\circ$ . In contrast to the small threshold amplitudes found by Herbert [7] for two-dimensional boundary layers, Balachandar et al. [1] determined threshold amplitudes of about 10% for the onset of secondary instabilities in three-dimensional boundary layers. Also in contrast to the transition in two-dimensional boundary layers, Balachandar et al. reported similar characteristics for the fundamental and the subharmonic secondary disturbance type.

Wintergerste and Kleiser [19] presented results from a temporal DNS computation of the transition process in the DLR Experiment. In the region of nonlinear saturation, they reported the development of a secondary crossflow vortex close to the wall, which is in qualitative agreement with the PSE results by Malik et al. [13]. Continuing their simulation further into the transition process, Wintergerste and Kleiser found that the secondary vortex initiated a vortex-splitting into smaller wavelength structures that caused the turbulent breakdown shortly thereafter.

A qualitatively new result indicating the existence of algebraically amplified modes in the otherwise convectively unstable Blasius boundary layer was presented by Koch [8]. Computing nonlinear equilibrium solutions at finite Reynolds numbers using numerical bifurcation theory, he examined the secondary instability of the such obtained modified mean flow using Floquet theory. In contrast to previous work, the nonlinear computation of the modified mean flow allowed him to omit the shape assumption. Investigating secondary disturbances that travel with the same phase speed as the primary disturbances (phase-locked), Koch found the existence of links between several unstable modes (coalescence) and of a modal degeneracy. The latter is defined as the coincidence of two or more eigenvalues and their eigenvectors that leads to a locally algebraic growth of these disturbances. It is this mechanism that might explain the experimentally observed explosive growth of high-frequency disturbances in the late stages of the transition process.

In summary of the presented review, the secondary instabilities are seen as high-frequency disturbances that originate from regions of high shear and vorticity away from the wall and that grow explosively within a short streamwise distance. Their frequency is usually in the kHz-range, which is an order-of-magnitude higher than the frequency of the most amplified primary traveling disturbances and in accordance with the typical local time scale  $t^* = \delta^*/U_e^*$  in the region of the nonlinear saturation. The explosive growth of

the high-frequency disturbances then initiates a break-up of the large-scale crossflow vortex structures into smaller wavelength vortices that is immediately followed by the breakdown to turbulence. From the above, it is clear how the secondary instability to high-frequency disturbances develops. Important open questions regard threshold amplitudes necessary for a self-sustained growth of the high-frequency disturbances, and the route by which the high-frequency disturbances enter the boundary layer before their amplitude is explosively amplified by the strong growth rates typical for the secondary instability.

In the present second part of this paper, we investigate the secondary instability of a mean flow that is modified by the presence of a stationary crossflow vortex using Floquet theory. The equilibrium solutions for the considered problems of Swept Hiemenz Flow and the DLR Transition Experiment are computed using the Parabolized Stability Equations (PSE), as described in Part 1. The formulation of the Floquet theory is introduced in Section two. Starting with a brief summary of the observations in Part 1, Section three presents results from a temporal analysis of the secondary instability of Swept Hiemenz Flow. Here, the emphasis is on the routes by which the secondary disturbances enter the boundary layer, and on their threshold amplitudes. Section four contains similar results for the DLR Experiment. There, however, the focus is on the existence of multiple eigenvalues in the region of nonlinear amplitude saturation.

**2. Floquet Theory.** A Floquet system is defined to be a system of linear ODE's whose coefficients are periodic in the independent variables. Floquet Theory was, for example, applied by Herbert [7] to explain the nonlinear transition process in two-dimensional boundary layers, by Reed [14] for a swept flat plate boundary layer, as well as by Fischer and Dallmann [5] for the DLR Transition Experiment.

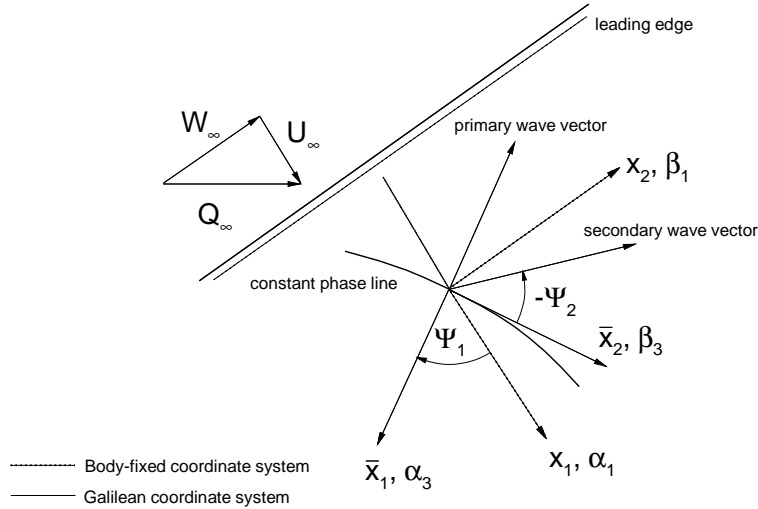


FIG. 2.1. *Coordinate systems and wave angle definitions*

Using Floquet theory, we investigate the stability of a new mean flow consisting of the original basic flow and the saturated primary disturbance wave. We define a new Galilean coordinate system  $(\bar{x}_1, \bar{x}_2, \bar{x}_3)$  that travels with the phase velocity in the  $\bar{x}_1$ -direction. The coordinate  $\bar{x}_2$  is aligned with the constant phase lines as shown in Figure 2.1. In this coordinate system, the new mean flow  $Q_2 = \{U_2, W_2, V_2, P_2\}^T$  is formed by a superposition of the parallel base flow  $Q_0(\bar{x}_3)$  and the solutions of the primary disturbance quantities

obtained from a PSE computation. In equation 2.1,  $\alpha_3$  is the real wave number in the  $\bar{x}_1$ -direction. Its defi-

$$(2.1) \quad Q_2(\bar{x}_1, \bar{x}_3) = Q_0(\bar{x}_3) + \sum_{m=-\infty}^{\infty} \hat{q}_{1_m}(\bar{x}_3) e^{im\alpha_3 \bar{x}_1}$$

$$(2.2) \quad \alpha_3 = \text{sgn}(\Psi) \sqrt{\alpha_{1,real}^2 + \beta_1^2} \ ; \ \Psi_1 = \tan^{-1}\left(\frac{\beta_1}{\alpha_{1,real}}\right)$$

nition is given in equation 2.2, where  $\Psi_1$  is the wave angle of the primary disturbances. By forming the mean flow  $Q_2$  as described above, the neglect of the mean flow distortion (shape assumption) and the assumption of an arbitrary amplitude of the primary disturbance utilized in previous work ([7], [5]) are avoided. The temporal stability of this mean flow is investigated by seeking a disturbance of the form shown in equation 2.3. There, the new vector of unknowns  $q_3$  consists of the four primitive variables  $u_3$ ,  $w_3$ ,  $v_3$  and  $p_3$ . Further, the real part of  $\sigma_3$  measures the growth of the secondary instability, its imaginary part determines the frequency, and  $\beta_3$  is the real wave number tangential to the constant phase lines.

$$(2.3) \quad q_3(\bar{x}_1, \bar{x}_2, \bar{x}_3, t) = e^{\sigma_3 t + i\beta_3 \bar{x}_2} \sum_{m=-\infty}^{\infty} \hat{q}_{3_m}(\bar{x}_3) e^{im\alpha_3 \bar{x}_1}$$

Substituting equations 2.1 and 2.3 for  $V_0$  and  $v_1$ , respectively, into the Navier-Stokes equations in disturbance form (see Part 1), dropping the nonlinear term  $(v_1 \cdot \nabla) v_1$  and introducing a new vector of unknowns  $\Lambda_m = \{\hat{u}_{3_m}, \partial \hat{u}_{3_m} / \partial \bar{x}_3, \hat{w}_{3_m}, \partial \hat{w}_{3_m} / \partial \bar{x}_3, \hat{v}_{3_m}, \hat{p}_{3_m}\}^T$ , we obtain a linear system of ODE's for the vector of the secondary disturbance eigenfunctions  $\Lambda$ . The resulting equations for all the Fourier modes are given in equations 2.4 - 2.17, where  $\Lambda$  is a  $6 \cdot (2 \cdot M + 1)$  vector at the normal location  $k$ .

$$(2.4) \quad \frac{\partial \Lambda_{1_m}}{\partial \bar{x}_3} = \Lambda_{2_m} \ ; \ \frac{\partial \Lambda_{3_m}}{\partial \bar{x}_3} = \Lambda_{4_m} \ ;$$

$$(2.5) \quad \frac{\partial \Lambda_{2_m}}{\partial \bar{x}_3} = \{\Delta \Lambda_{1_m} + im\alpha_{3_m} \Lambda_{6_m} + (\sum_{m_1} U_{2_{m_1}})(\sum_{n_1} in_1 \alpha_{3_{n_1}} \Lambda_{1_{n_1}}) +$$

$$(2.6) \quad (\sum_{m_1} W_{2_{m_1}})(i\beta_3 \sum_{n_1} \Lambda_{1_{n_1}}) + (\sum_{m_1} V_{2_{m_1}})(\sum_{n_1} \Lambda_{2_{n_1}}) +$$

$$(2.7) \quad (\sum_{m_1} \Lambda_{1_{m_1}})(\sum_{n_1} in_1 \alpha_{3_{n_1}} U_{2_{n_1}}) + (\sum_{m_1} \Lambda_{5_{m_1}})(\sum_{n_1} \frac{\partial U_{2_{n_1}}}{\partial \bar{x}_3})\} Re \ ;$$

$$(2.8) \quad \frac{\partial \Lambda_{4_m}}{\partial \bar{x}_3} = \{\Delta \Lambda_{3_m} + i\beta_3 \Lambda_{6_m} + (\sum_{m_1} U_{2_{m_1}})(\sum_{n_1} in_1 \alpha_{3_{n_1}} \Lambda_{3_{m_1}}) +$$

$$(2.9) \quad (\sum_{m_1} W_{2_{m_1}})(i\beta_3 \sum_{n_1} \Lambda_{3_{n_1}}) + (\sum_{m_1} \Lambda_{4_{m_1}})(\sum_{n_1} V_{2_{n_1}}) +$$

$$(2.10) \quad (\sum_{m_1} \Lambda_{1_{m_1}})(\sum_{n_1} in_1 \alpha_{3_{n_1}} W_{2_{n_1}}) + (\sum_{m_1} \Lambda_{5_{m_1}})(\sum_{n_1} \frac{\partial W_{2_{n_1}}}{\partial \bar{x}_3})\} Re \ ;$$

$$(2.11) \quad \frac{\partial \Lambda_{5_m}}{\partial \bar{x}_3} = -im\alpha_3 \Lambda_{1_m} - i\beta_3 \Lambda_{3_m} \ ;$$

$$(2.12) \quad \frac{\partial \Lambda_{6_m}}{\partial \bar{x}_3} = -\Delta \Lambda_{5_m} - \frac{1}{Re}(im\alpha_{3_m} \Lambda_{2_m} + i\beta_3 \Lambda_{4_m}) -$$

$$(2.13) \quad (\sum_{m_1} U_{2_{m_1}})(\sum_{n_1} in_1 \alpha_{3_{n_1}} \Lambda_{5_{n_1}}) - (\sum_{m_1} W_{2_{m_1}})(i\beta_3 \sum_{n_1} \Lambda_{5_{n_1}}) +$$

$$(2.14) \quad (\sum_{m_1} V_{2_{m_1}})(\sum_{n_1} in_1 \alpha_{3_{n_1}} \Lambda_{1_{n_1}}) + (\sum_{m_1} V_{2_{m_1}})(i\beta_3 \sum_{n_1} \Lambda_{3_{n_1}}) -$$

$$(2.15) \quad \left( \sum_{m_1} \Lambda_{I_{m_1}} \right) \left( \sum_{n_1} i n_1 \alpha_{3_{n_1}} V_{2_{n_1}} \right) - \left( \sum_{m_1} \Lambda_{5_{m_1}} \right) \left( \sum_{n_1} \frac{\partial V_{2_{n_1}}}{\partial \bar{x}_3} \right) ;$$

$$(2.16) \quad \Delta = \frac{1}{Re} (m^2 \alpha_{3_m}^2 + \beta_3^2) + \sigma_3 ;$$

$$(2.17) \quad \frac{\partial \Lambda}{\partial \bar{x}_3} = \bar{A} \Lambda$$

Collecting terms with the same Fourier component, writing equations 2.4 - 2.16 in the entire wall-normal domain, and employing a fourth-order-accurate compact scheme formulation, we obtain a generalized eigenvalue problem of the form given in equation 2.18. In fact, the two-point, fourth-order accurate compact scheme formulation applied here ([12]) yields the non-trivial case of a singular, non-symmetric, and semi-positive-definite generalized eigenvalue problem. The leading dimensions of the coefficient matrices  $\bar{A}$  and  $\bar{B}$  in equation 2.18 can easily reach significant orders. For example, considering a minimal problem size for a satisfactory resolution in both the Fourier space and the wall-normal direction, a leading matrix dimension of  $9.6 \cdot 71 = 3834$  is obtained by distributing 71 points in the normal direction and truncating the Fourier series at  $M=4$ . Hence, the need for efficient eigenvalue solvers is obvious.

$$(2.18) \quad \bar{A} \Lambda = \sigma_3 \bar{B} \Lambda$$

Utilizing the QZ-algorithm that is implemented in the ZGEGV-routine available in the public-domain software library LAPACK proved to be extremely CPU-time intensive for these matrix dimensions. For example, it takes about five CPU-hours on a Sun-Ultra-2 workstation (333 MHz) to compute the entire eigenvalue spectrum of a problem with a leading matrix dimension of 2700. Therefore, we adapted the recently developed Implicitly Restarted Arnoldi Method ([11]) to the present problem. The method is available as a part of the public-domain software library ARPACK. It approximates the eigenvalues and eigenvectors in specified regions of the eigenvalue spectrum. Applying this method to a problem size of 5000, the required CPU-time to compute 10 eigenvalues that are located in a selected region of interest amounts to only one minute on the workstation quoted above.

For a confirmation of the eigenvalues obtained from the global solver, we developed a local eigenvalue solver based on a Newton-Raphson technique. The solution method is based on a two-point, fourth-order-accurate compact scheme formulation ([12]), and the solution algorithm allows for several iteration options in order to account for the presence of  $(2 \cdot M + 1)$  eigenmodes in the coefficient matrices. The iteration is performed at the wall-normal location where the most dominant secondary eigenmode has its maximum. There, we drop either one of the momentum equations, or the continuity equation, solve the block-tridiagonal system, and check the convergence by evaluating the dropped momentum, or continuity equation. Hence, the developed solution method is capable of iterating on different eigenmodes of the unknowns  $u_3$ ,  $w_3$  and  $v_3$  at a specified wall-normal location.

**3. Swept Hiemenz Flow.** Provided that a mean flow exists that is modified by a saturated crossflow vortex, the secondary instability originates from the locations of high shear and vorticity away from the wall. This is seen in Figure 3.1 where we plot the vorticity of the total flow quantity  $Q_2$  that is computed according to equation 3.1.

$$(3.1) \quad |\Omega| = \sqrt{\left( \frac{\partial W_2}{\partial x_3} \right)^2 + \left( \frac{\partial V_2}{\partial x_2} \right)^2 + \left( \frac{\partial W_2}{\partial x_1} \right)^2 + \left( \frac{\partial U_2}{\partial x_2} \right)^2 + \left( \frac{\partial V_2}{\partial x_1} \right)^2 + \left( \frac{\partial U_2}{\partial x_3} \right)^2}$$

At the streamwise location of  $Re=643.5$ , a high vorticity concentration is seen at normal locations between  $x_3 \simeq 1$  and  $x_3 \simeq 2$ , which corresponds to about half the boundary layer thickness. Also seen are

the footprint of the stationary primary crossflow vortex at the wall that corresponds to the streaks of oil or china-clay observed in experiments, as well as a developed secondary crossflow vortex close to the wall that shows as  $\lambda$ -shape structure at  $Re=643.5$ .

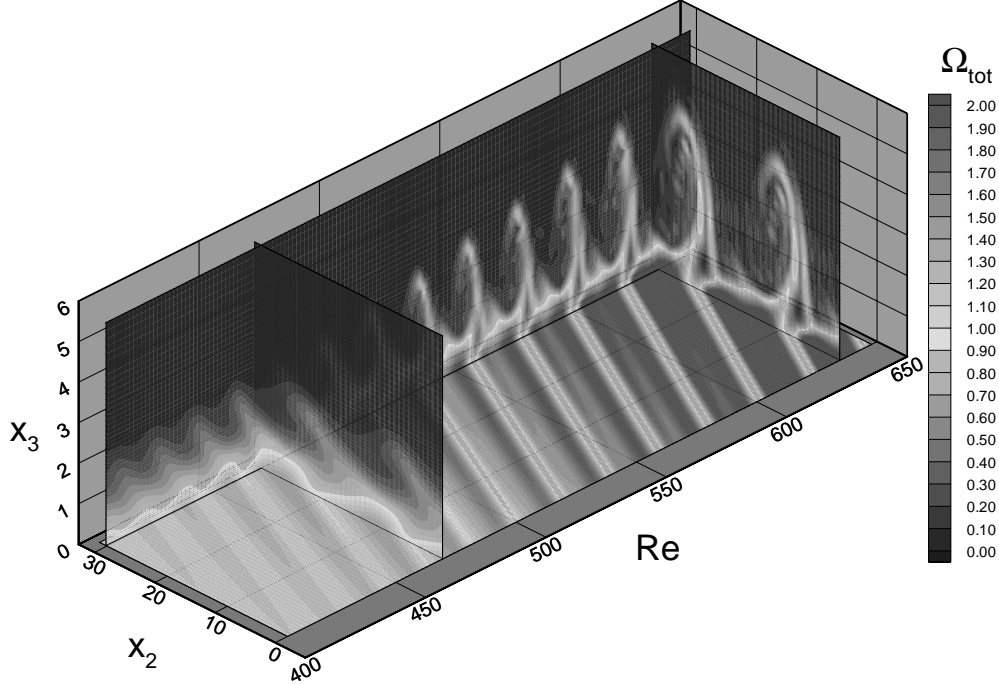


FIG. 3.1. *Total vorticity in the presence of a stationary crossflow vortex*

The temporal investigation of the secondary instability is started at the streamwise location where  $Re=546$ . At this location, the stationary disturbance of an initial amplitude  $\hat{A}_s=0.1\%$  has fully saturated and reached an amplitude level of  $\hat{A}_s=24\%$  for the  $u_1$ -component (see Figure 3.2 in Part 1). The computations presented here are limited to a maximal number of eight modes ( $m = -8, \dots, 8$ ) in the Fourier approximation. However, Malik et al. [13] showed that including 16 modes does not change the results qualitatively. Further, the results presented consider the fundamental type of secondary disturbances only. This restriction of the work is supported by the findings of Balachandar et al. [1] for the three-dimensional boundary layer of a rotating-disc flow where they did not find a qualitative difference between the behavior of fundamental and subharmonic secondary disturbances.

The computational grid applied in the present computations is described as follows. For the same computational domain as in Part 1, where the freestream boundary conditions were enforced at a normal extension of about 10 boundary layer thicknesses, the total number of points is decreased from 141 to 81. Also, the grid is now stretched in the entire domain according to equation 3.2 such that the number of points within the boundary layer is 50. For the local solution method, the iteration can be performed on either the continuity equation, or one of the momentum equations. Additionally, the disturbance mode to be iterated

$$(3.2) \quad \bar{x}_3 = \frac{\Delta \cdot \eta}{1 + \frac{\Delta}{\bar{x}_{3,max}} - \eta}$$

on can be specified. Table 1 presents the findings from a grid refinement study. Shown are results from the local method for different grids and iteration options. The guess values from the second-order-accurate

global method for the two different numbers of points are given by  $\sigma_3=(0.0267,-1.2043)$  for 71 points, and  $\sigma_3=(0.0262,-1.2073)$  for 81 points. The results of the fourth-order-accurate local method vary only in the fourth decimal place, and thus, the grid resolution is considered satisfactory.

TABLE 3.1  
*Grid study at  $Re=546$ ,  $\alpha_3=-0.508$ ,  $\beta_3=0.9$ ,  $Mode=-1$*

$\Delta$	Points	Equation	$\bar{x}_{3,max}$	$\sigma_3$
3	71	continuity	44	(0.021652,-1.212607)
3	71	$\bar{x}_3$ -mom.	44	(0.021652,-1.212607)
5	71	continuity	44	(0.021779,-1.212359)
5	71	$\bar{x}_3$ -mom.	44	(0.021779,-1.212359)
3	81	continuity	55	(0.021715,-1.212264)
5	81	continuity	55	(0.021729,-1.212671)

In general, there will be several unstable eigenmodes for a given wave number at a streamwise location. Thus, a scan of the complex  $\sigma_3$ -plane for a wave number of  $\beta_3=0.8$  is performed first. Here, the global method provides the guess values that are checked for using the local solver. All eigenvalues that were found within the scanned domain are plotted in Figure 3.2. Even though they appear clustered around  $\sigma_3=(0,-1.)$ , there

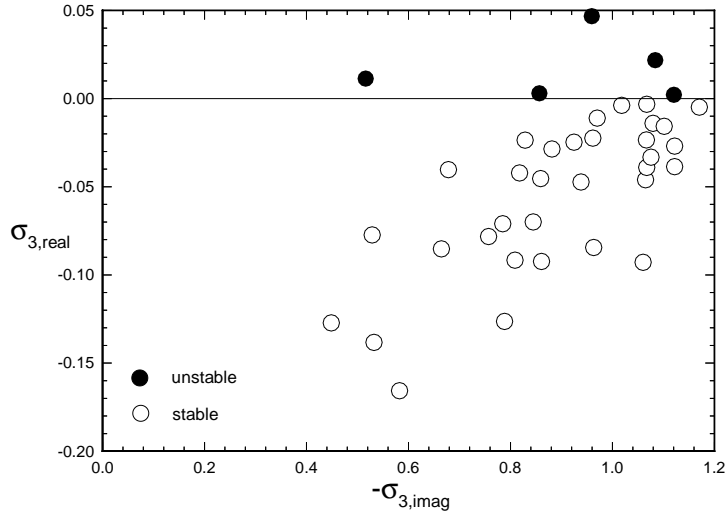


FIG. 3.2. *Temporal eigenvalue spectrum at  $Re=546$*

is no obvious connection between the positive (unstable) real parts. For the chosen parameters, this isolated appearance indicates that there are no multiple eigenvalues present in the flow. The five detected unstable eigenvalues are given in the order of increasing frequency in Table 3.2. It is seen that the unstable secondary frequencies are an order-of-magnitude higher than the frequency considered in Part 1 ( $F=0.75 \cdot 10^{-4}$ ).

The shape-functions of the five unstable modes are shown in Figure 3.3. Plotted is the summation of eight Fourier components of the wave number  $\alpha_3$  in the Galilean coordinate system. It is observed that the shape-functions of the different modes vary widely in features like the location of the maximum in the normal direction, the largest disturbance component, the magnitude, the presence of multiple peaks, and the



TABLE 3.2  
Unstable eigenvalues  $Re=546$ ,  $\alpha_3=-0.508$ ,  $\beta_3=0.8$

Mode	$\sigma_3$	$F=-\sigma_{3,imag}/\bar{Re}$
1	(0.0113,-0.5160)	$1.03 \cdot 10^{-3}$
2	(0.0030,-0.8566)	$1.71 \cdot 10^{-3}$
3	(0.0467,-0.9595)	$1.92 \cdot 10^{-3}$
4	(0.0218,-1.0838)	$2.16 \cdot 10^{-3}$
5	(0.0021,-1.1205)	$2.24 \cdot 10^{-3}$

extension into the outer flow. Of special interest are Modes 4 and 5, as well as the most unstable Mode 3. Because of their full shape-profiles, Modes 4 and 5 might be easier detected in experiments than the other three modes that show a more narrow and fluctuating shape. For Mode 4, in particular, it is noted that the component tangential to the constant phase lines has a shape that is very similar to the experimentally and numerically observed profile in the DLR Transition experiment at  $x_1/c=0.80$  (Fischer and Dallmann [5]). For that reason, most of the following studies consider Mode 4.

In Figure 3.4, the shape-functions of the individual Fourier components are given for Mode 4. Plotted are the normalized quantities for the first seven modes. It is observed that the disturbance component tangential to the constant phase lines (0-Mode) shows a double peak structure for both wall-parallel disturbance quantities. The maximal disturbance quantity is found for the  $\hat{w}_3$ -component at  $\bar{x}_3 \simeq 3$ , where its normalized value  $|\hat{w}_{3,0}|/|\hat{w}_{3,total}|_{max} \simeq 1$ .

While studying the origin of the secondary instability, other important questions address the existence of a link between the eigenmodes of the undisturbed mean flow, investigated by the linear stability theory, and the unstable secondary eigenmodes, investigated by Floquet theory, and also the magnitude of the threshold amplitudes at which the secondary disturbances become unstable. In order to investigate these questions, the amplitude of the stationary disturbances obtained from the nonlinear stability analysis in the previous section is set to  $A=1.0$  for the given Reynolds number. Then, by gradually decreasing  $A$  to zero, the variation of the eigenvalues is monitored. During the computations, the evolution of the shape-functions is followed in order to assure that no jumps to different eigenvalues occur. A typical step size in the amplitude is  $\Delta A=0.01$ , and the computations are continued until the local method ceases to converge.

For a Reynolds number of  $Re=546$ , a value of  $A=1$  corresponds to amplitudes of  $\hat{A}_s=24\%$ ,  $\hat{A}_s=17\%$  and  $\hat{A}_s=1\%$  for the  $u_1$ -,  $w_1$ - and  $v_1$ -disturbance components of the primary stationary vortex, respectively. In Figure 3.5, the variation of the eigenvalues  $\sigma_3=(\sigma_{3,real}, \sigma_{3,imag})$  versus a decreasing amplitude  $A$  is shown for the five unstable eigenvalues at  $A=1$ . Additionally, the eigenvalues of the undisturbed parallel mean flow  $Q_0(\bar{x}_3)$  are shown in the relevant  $\sigma_3$ -range. It turns out that only one of the five unstable eigenvalues at  $Re=546$  has a link to the eigenvalue spectrum of the undisturbed mean flow. This connection could be established for Mode 1, the mode with the lowest unstable secondary frequency ( $F=1.03 \cdot 10^{-3}$ ). As seen in Figure 3.5, the variation of the eigenvalues with decreasing amplitude  $A$  takes very different routes. For example, the highest frequency mode (Mode 5) becomes stable at a threshold amplitude of  $A_{thres}=0.98$ . Shortly thereafter, the iteration for an eigenvalue ceases to converge. On the other hand, Modes 2 and 3 could be followed further until  $A \simeq 0.1$ . The threshold amplitudes for Modes 1-4, respectively, are  $A_{thres}=0.88$ ,  $A_{thres}=0.95$ ,  $A_{thres}=0.31$ ,  $A_{thres}=0.55$ . Thus, this analysis predicts the onset of a secondary instability due to Mode 3 already for stationary disturbance amplitudes of  $\hat{A}_s=0.31 \cdot 24\%=7.5\%$  and  $\hat{A}_s=0.31 \cdot 17\%=5\%$  for the  $u_1$ - and  $w_1$ -components, respectively. The corresponding values for Mode 4 are  $\hat{A}_s=0.55 \cdot 24\%=13\%$  and

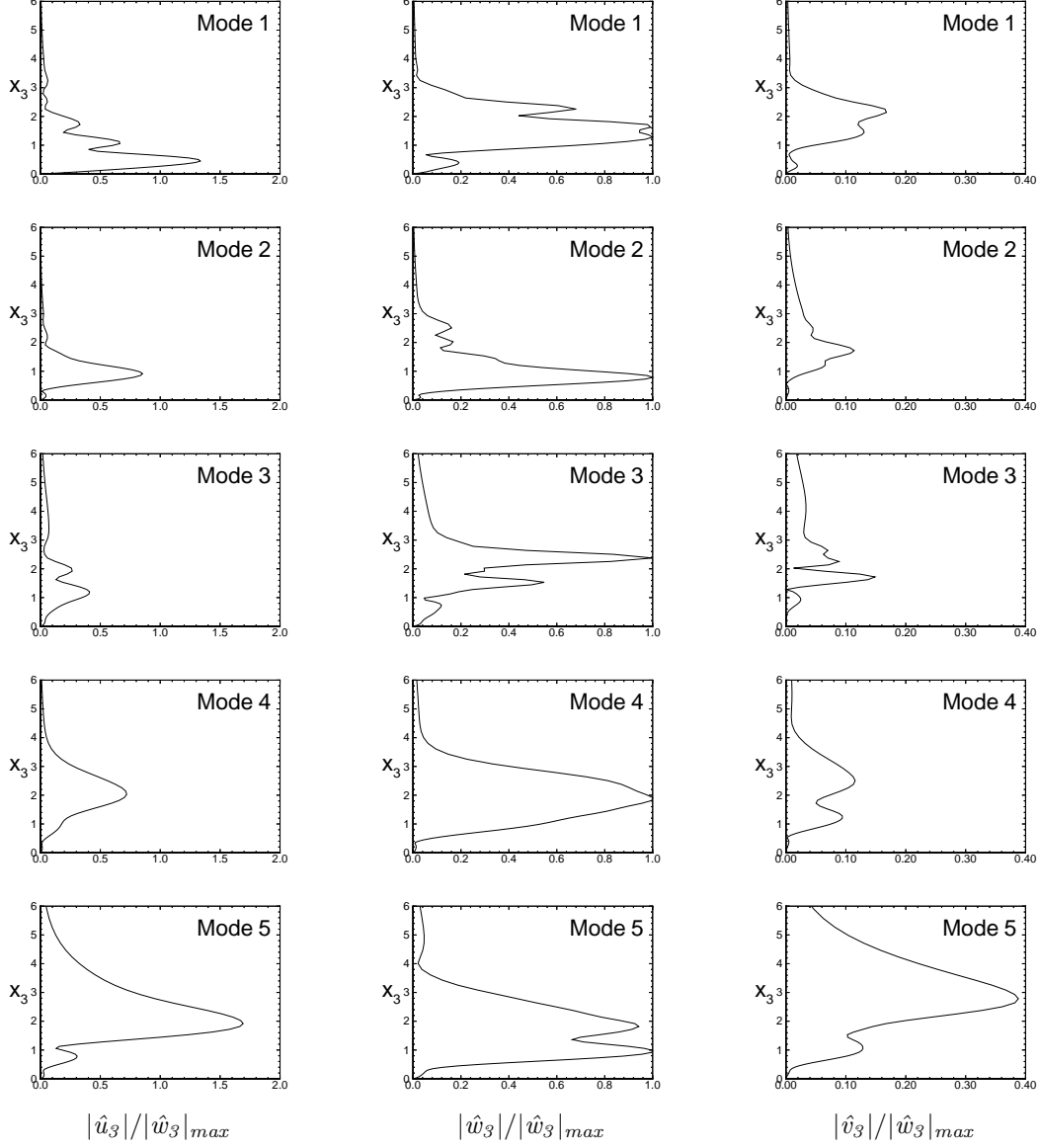


FIG. 3.3. Total shape-functions for unstable modes at  $Re=546$ ,  $\alpha_3=-0.508$ ,  $\beta_3=0.8$

$\hat{A}_s=0.55 \cdot 17\%=9\%$ .

In order to investigate the eigenmode variation in the amplitude range where the eigenvalue computation stops converging, the next study examines the decay of the individual disturbance components at the freestream boundary. Thereby, it can be determined whether the convergence problems are due to an insufficient grid resolution, or if they are part of the physics of the investigated problem. In the present stability formulation, a complex eigenvalue reaches the continuous spectrum when the corresponding eigenfunction does not decay in the freestream and is of rather oscillatory nature ([2]). In the following, the method of the investigation is described, and results are presented for the Modes 1 and 4.

In Floquet theory, we seek a solution to the linear eigenvalue problem that is written as in equation 2.17 (see Section two), where the elements of the coefficient matrix  $\bar{A}$  are determined from a nonlinear PSE computation. Since the coefficients of the matrix are not constant in the entire domain, one usually solves

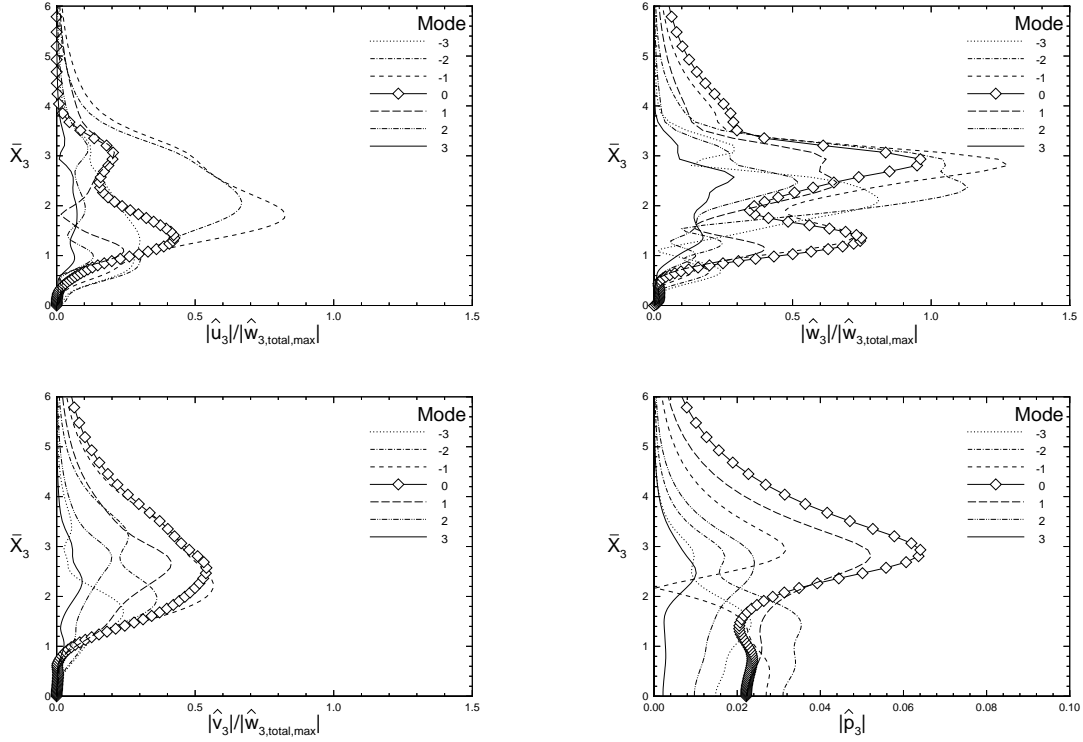


FIG. 3.4. Shapes of the secondary instability eigenfunctions for Mode 4 at  $Re=546$

the eigenvalue problem using a Newton-Raphson technique. Here, however, the focus is on the eigenvalues of  $\bar{A}$  at the freestream boundary where the primary disturbance quantities are zero, and thus, the coefficients of the matrix  $\bar{A}$  are constant. Therefore, the behavior of the secondary disturbances at the freestream boundary can be investigated by finding the eigenvalues of the submatrix  $\bar{A}_n$  at the maximal normal extension of the computational domain. The dimension of the submatrix  $\bar{A}_n$  depends on the number of considered Fourier modes in the Floquet analysis and is determined to  $(2 \cdot M + 1) \cdot 6$  for the six components of the vector of unknowns (see Section two). Considering eight Fourier modes in the analysis, the complex and non-symmetric coefficient matrix  $\bar{A}_n$  consists of  $102 \times 102$  elements. If the eigenvalue problem to be solved is well-posed, one obtains 51 positive and 51 negative eigenvalues which are distributed almost symmetrically about the imaginary axis. In Figure 3.6a), the eigenvalue spectrum at the freestream boundary of Mode 4 is shown for an amplitude of  $A=1$ . In that case, none of the eigenvalues has a zero real part, the secondary disturbances decay in the freestream, and the iteration for an eigenvalue of the entire problem converges.

TABLE 3.3  
Eigenvalue characteristics at the freestream boundary for Mode 4

$A$	1.0	0.8	0.6	0.4	0.38	0.36	0.34
# of $\lambda_{real,i} > 0$	51	51	51	51	51	51	53
# of $\lambda_{real,i} < 0$	51	51	51	51	51	51	49
$(\lambda_{real,i})_{min}$	0.8	0.8	0.8	-0.16	-0.078	-0.011	0.0066

When approaching the continuous spectrum, however, the real part of the eigenvalue closest to the imaginary axis tends towards zero, and the well-posedness of the eigenvalue problem is violated by an

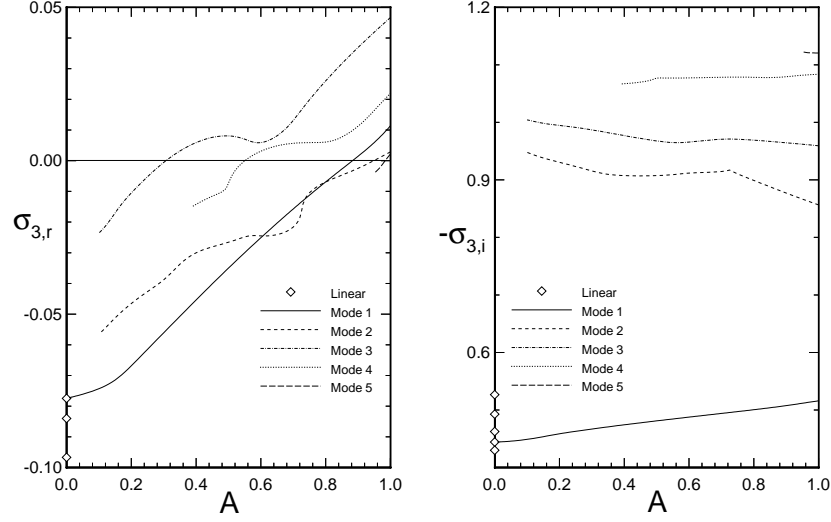


FIG. 3.5. Growth rates and frequencies of the secondary disturbances vs. the amplitude  $A$  ( $Re=546$ ,  $\alpha_3=-0.508$ ,  $\beta_3=0.8$ )

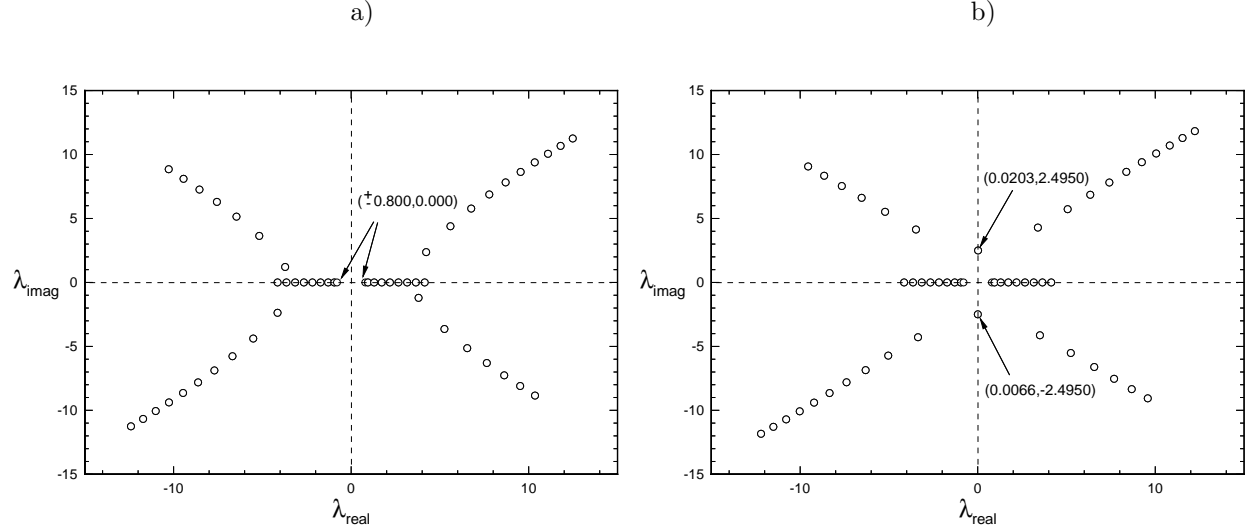


FIG. 3.6. Eigenvalue spectra at the freestream boundary for Mode 4 ( a)  $A=1$ , b)  $A=0.34$ )

imbalance of the eigenvalues with a positive and negative part. This is seen in Figure 3.6b), where the eigenvalue spectrum at the freestream boundary of Mode 4 is shown for an amplitude of  $A \simeq 0.34$ . There are two eigenvalues close to the imaginary axis which indicates that the disturbances do not decay in the freestream. Further, tables 3 and 4 list the number of eigenvalues with positive and negative real parts in the spectrum, as well as the magnitude of the eigenvalues closest to the imaginary axis for the Modes 1 and 4 in dependence of the amplitude  $A$ . It is seen that the eigenvalues of Mode 4 join the continuous spectrum at an amplitude of  $A=0.34$ , whereas the Mode 1 indeed reaches the linear eigenvalue spectrum, as stated earlier.

In Figure 3.7, the normalized total shape-functions of the  $w_3$ -component of Mode 1 are given for different

TABLE 3.4  
Eigenvalue characteristics at the freestream boundary for Mode 1

$A$	1.0	0.8	0.6	0.4	0.2	0.1	0.01
# of $\lambda_{real,i} > 0$	51	51	51	51	51	51	51
# of $\lambda_{real,i} < 0$	51	51	51	51	51	51	51
$(\lambda_{real,i})_{min}$	0.8	0.8	0.8	0.8	0.8	0.8	0.8

amplitudes. It is seen that the shape-functions for the different amplitudes indeed belong to the same family of eigenmodes. Comparing the linear shape-function with the nonlinear shape-function at  $A=0.01$ , it is obvious that nonlinear and linear results merge in the limit of  $A \rightarrow 0$ .

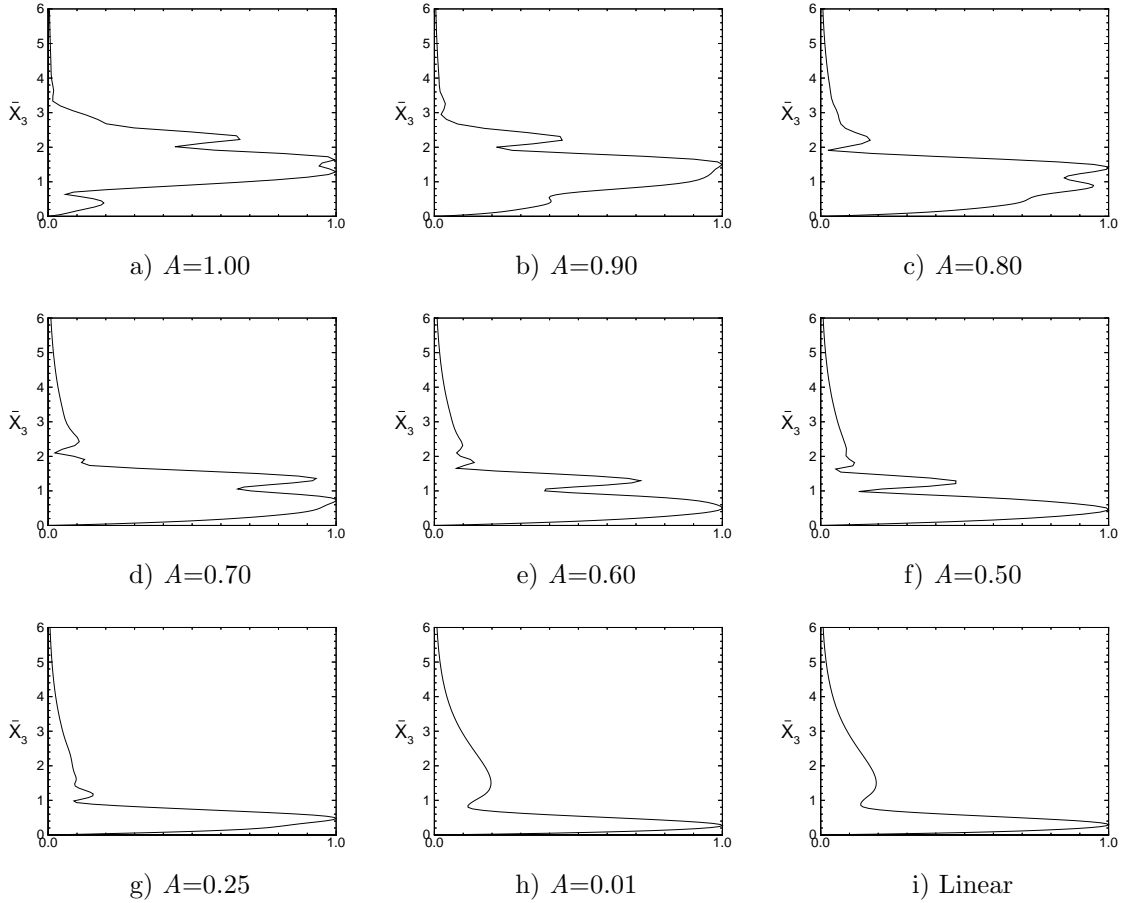


FIG. 3.7. Shape-functions  $|\hat{w}_3|/|\hat{w}_{3,max}|$  of the linear eigenmode and of Mode 1 for various amplitudes  $A$

Next, the eigenvalues  $\sigma_3$  for the different unstable modes are computed as functions of the wave number tangential to the stationary vortex at  $Re=546$ . In particular, three of the five unstable eigenmodes at  $\beta_3=0.8$  are traced through their unstable wave number range. Figures 3.8 and 3.9 show the growth rate and frequency development, respectively, that was obtained by closely watching the evolution of the eigenfunctions with changing wave numbers. Thereby, it is assured that the curves for the different modes in Figure 3.8 indeed belong to the specified modes.

From Figures 3.8 and 3.9, the following observations can be made. A wide range of unstable secondary

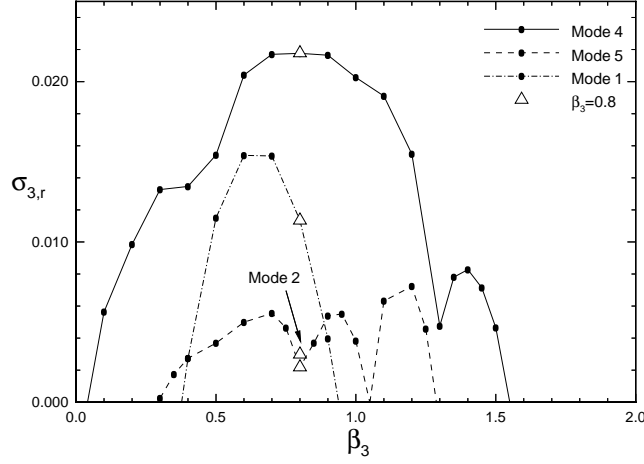


FIG. 3.8. Secondary growth rates at  $Re=546$

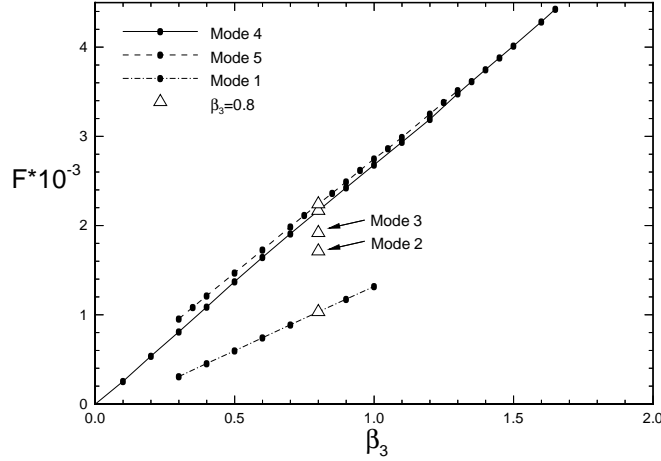


FIG. 3.9. Secondary frequencies at  $Re=546$

wave numbers is present at the investigated Reynolds number. Starting at  $\beta_3=0$ , which corresponds to an alignment with the primary wave vector, the disturbances turn towards the direction of the constant phase lines with a growing wave number tangential to the stationary vortex. The dependence of the frequency on the wave number  $\beta_3$  is approximately linear, which corresponds to a constant phase speed of the disturbances. An intricate structure of the high-frequency/low-growth rate Mode 5 is observed. The growth rate behaves in a periodic manner as a fraction of the wave number  $\beta_3$ . The most unstable disturbances of Modes 4 and 5 are found in the wave number range of  $\beta_3=0.6 - 0.9$ . This corresponds to an inclination of the secondary structures of  $\Psi_2=-30^\circ \dots -40^\circ$  with respect to the direction of the constant phase lines. The Modes 4 and 5 have very similar frequencies; however, the frequency curves never cross each other. Even though the curves for the real parts (growth rates) of the different modes do cross each other, their eigenvalues  $\sigma_3=(\sigma_{3,real}, \sigma_{3,imag})$  do not coincide because of the missing corresponding crossovers of the imaginary parts (frequencies). Thus, multiple eigenvalues were not detected at the investigated location.

In order to gain more insight into the spatial development of the secondary instability, a temporal analysis at eight different streamwise positions is performed. Choosing Mode 4 at  $Re=546$  and decreasing the Reynolds number, this mode is traced back to its onset at  $Re \simeq 475$ . There, the amplitude level of both the  $u_1$ - and the  $w_1$ -components of the stationary vortex is  $\hat{A}_s=11\%$ , which closely corresponds to the results obtained by decreasing the amplitude  $A$  for Mode 4 (see Figure 3.5). Figure 3.10 shows the secondary growth rates at the different streamwise positions. It can be seen that the unstable spanwise wave numbers align more closely with the direction of the wave vector  $k_{real}$  for a decreasing Reynolds number.

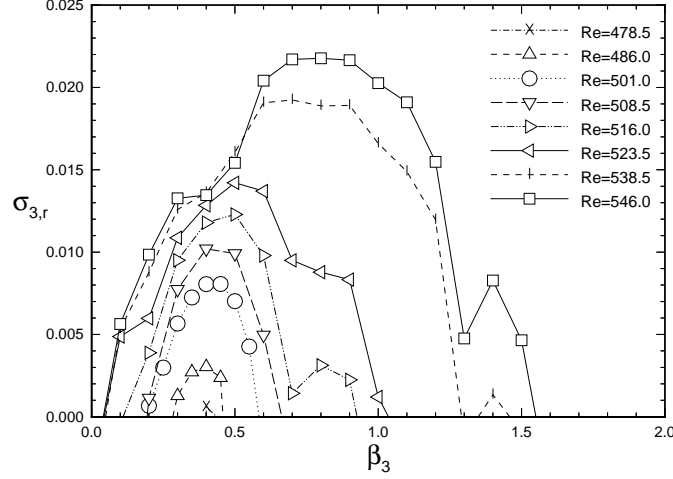


FIG. 3.10. Secondary growth rates at different streamwise stations (Mode 4)

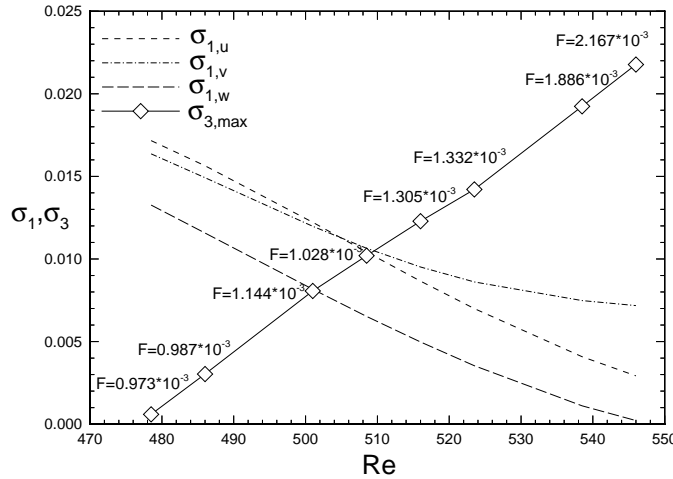


FIG. 3.11. Trace-back of the secondary instability (Mode 4)

In Figure 3.11, the most amplified secondary growth rates are plotted together with the primary growth rates. The most unstable secondary frequencies are found in the range of  $F=1.0 \cdot 10^{-3}$ - $2.0 \cdot 10^{-3}$ , which is an order-of-magnitude higher than the most amplified primary frequency of  $F=1.0 \cdot 10^{-4}$ . Also, a linear

development of the temporal growth rate  $\sigma_{3,real}$  is observed. Table 5 shows the wave numbers  $\alpha_3$ , the secondary growth rates, the wave numbers  $\beta_3$ , the wave angles of the secondary disturbances according to the definition in Section two, as well as the dimensional frequencies of the points of maximal amplification at the considered Reynolds number locations.

TABLE 3.5  
*Parameters for the most unstable disturbances of Mode 4*

$Re$	$\alpha_3$	$\sigma_{3,real,max}$	$\beta_{3,\sigma_3=max}$	$\Psi_{2,\sigma_3=max}$	$F_{\sigma_3=max} \cdot 10^3$
546.0	-0.508	0.0218	0.80	-32.4°	2.167
538.5	-0.510	0.0192	0.70	-36.1°	1.886
523.5	-0.513	0.0142	0.50	-45.7°	1.332
516.0	-0.515	0.0123	0.50	-45.8°	1.305
508.5	-0.517	0.0102	0.40	-52.3°	1.028
501.0	-0.519	0.0081	0.45	-49.1°	1.144
486.0	-0.524	0.0030	0.40	-52.6°	0.987
478.5	-0.527	0.0006	0.40	-52.8°	0.973

Another interesting feature in Figure 3.11 is the development of the primary and secondary growth rates. At  $Re \simeq 510$ , the primary and secondary growth rates are of the same order. At  $Re=546$ , however, the primary growth rates are about to become stable, whereas the temporal theory predicts a continued steep growth of the high-frequency disturbances. Looking at Figure 3.1 in Part 1 where the amplitude evolution of the stationary disturbances was plotted, we note that the onset of the secondary instability according to the temporal theory occurs at a location where the stationary disturbances start to saturate, and both the  $u_1$ - and the  $w_1$ -components of the stationary primary disturbance have reached an amplitude level of  $\hat{A}_s=11\%$ .

**4. DLR Transition Experiment.** In this section, results from a temporal analysis using Floquet theory performed at the chordwise location of  $x_1/c=0.6$  are presented. At this location, the averaged stationary disturbance component tangential to the inviscid streamline  $u_{tang,avg}$  with an initial amplitude of  $A_s \simeq 0.1\%$  at  $x_1/c=0.1$  has reached an amplitude level of  $A_s=20\%$  and is almost saturated. Special attention will be directed towards the existence of multiple eigenvalues in the considered region of nonlinear saturation that might explain the experimentally observed time-dependent occurrences of an explosive growth of traveling disturbances ([4]).

Pursuing the sequence of global and local eigenvalue computations as described in Section three, we find that there are more unstable eigenvalues present at this location than detected for Swept Hiemenz Flow at the investigated locations. The results for the secondary growth rates and frequencies of three selected modes are plotted in Figures 4.1 and 4.2. The unstable eigenvalues appear densely clustered in the wave number range between  $\beta_3=0.1$  and  $\beta_3=0.4$ . The disturbances with these wave numbers have frequencies of  $f^*=500$  Hz up to  $f^*=4000$  Hz (see Figure 4.2). The development of the eigenfunctions with a varying wave number tangential to the constant phase lines  $\beta_3$  was followed closely in order to assure that the plotted eigenvalues indeed belong to the same family of unstable secondary eigenmodes. In contrast to Swept Hiemenz Flow, where neither multiple eigenvalues, nor crossing growth rate curves could be found at the investigated locations, it can be seen in Figure 4.1 that the growth rate curves of the different modes cross. This indicates that the algebraically unstable modes found by Koch [8] for Blasius boundary layer flow might be also present in this three-dimensional boundary layer flow. Table 6 lists the secondary growth



rates, the wave numbers  $\beta_3$ , the wave angles of the secondary disturbances according to the definition in Section two, as well as the dimensional frequencies at the points of maximal amplification for the considered modes. It is observed that the wave angle range of the most amplified secondary disturbances agrees with the results for Swept Hiemenz Flow.

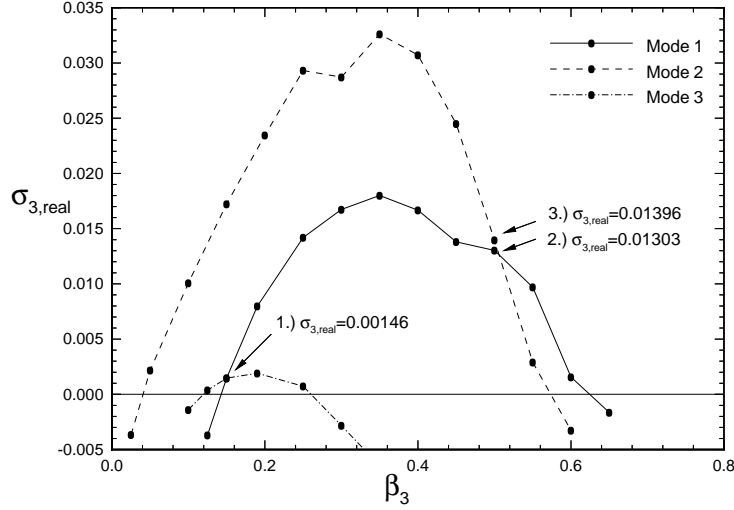


FIG. 4.1. Secondary growth rates at  $x_1/c=0.6$

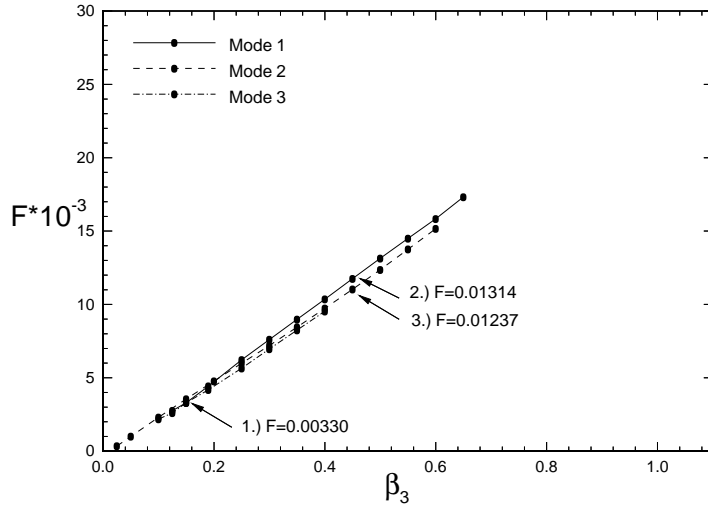


FIG. 4.2. Secondary frequencies at  $x_1/c=0.6$

Further, Figure 4.3 shows the total shape-functions of the most unstable secondary modes at  $x_1/c=0.6$ . Plotted are the normalized shape-functions of the disturbance velocity components for the most amplified wave numbers  $\beta_3$ . Comparing the shape-functions of the unstable modes in the Swept Hiemenz Flow problem at  $Re=546$  and  $\beta_3=0.8$  (see Figure 3.3) with the shape-functions shown in Figure 4.3, the following is noted. First, the shape-functions at  $Re=546$  are fuller than the profiles obtained here. This is attributed to the

TABLE 4.1  
Parameters for the most unstable modes at  $x_1/c=0.6$ , ( $\alpha_3=-0.201$ )

	$\sigma_{3,real,max}$	$\beta_{3,\sigma_3=max}$	$\Psi_{2,\sigma_3=max}$	$f_{\sigma_3=max}^*$ [Hz]
Mode 1	0.018001	0.35	-29.9°	3117
Mode 2	0.032616	0.35	-29.9°	2933
Mode 3	0.001906	0.19	-46.6°	1451

higher amplitude level of the stationary disturbances in the Swept Hiemenz Flow problem ( $\hat{A}_{s,u}=24\%$  at  $Re=546$ ;  $A_{s,u}=20\%$  at  $x_1/c=0.6$ ). Second, all the shape-functions at  $x_1/c=0.6$  show a strong maximum at a height of  $\bar{x}_3 \simeq 1$  mm, which is equivalent to about 30% of the boundary layer thickness at this location and can be interpreted as a formation of shear layers near  $\bar{x}_3 \simeq 1$  mm.

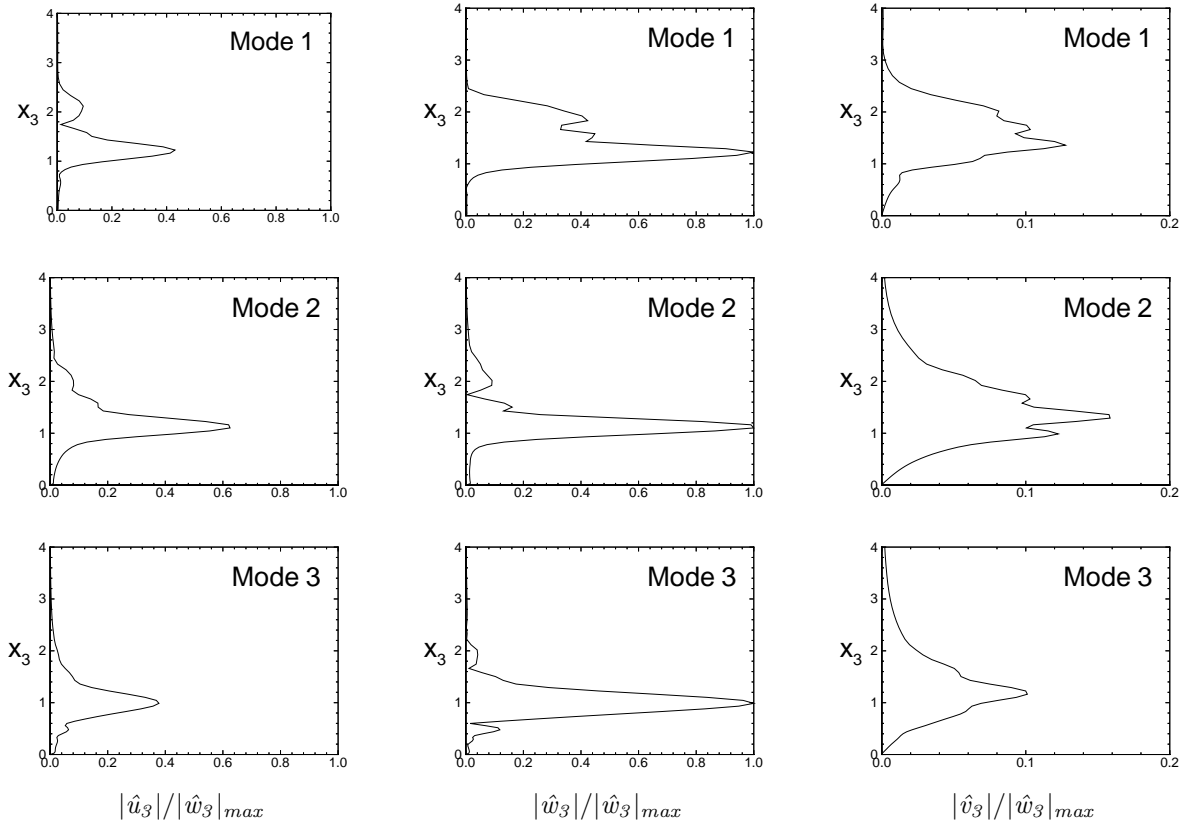


FIG. 4.3. Total shape-functions of the most unstable modes at  $x_1/c=0.6$ , ( $\alpha_3=-0.201$ , normal axis in millimeters)

From Figure 4.2 and as observed for Swept Hiemenz Flow, it appears that a linear frequency dependence on the wavenumber  $\beta_3$  can serve as a first guess for a distinction of the different modes. For closely clustered eigensolutions, however, only an additional comparison of the eigenfunctions can be a conclusive test. It is also noted from Figure 4.2 that the frequency curves of Modes 1 and 3 cross at the same wave number  $\beta_3=0.15$  as the corresponding growth rate curves in Figure 4.1 (see Point 1.). Hence, the existence of a multiple eigenvalue at this wave number needs further investigation. The temporal wave number at the location where Modes 1 and 3 cross is  $\sigma_3=(0.00146,-0.33792)$ . This corresponds to a dimensional frequency of  $f^*=1145$  Hz, which is about six times the most amplified frequency. In contrast, the dimensional frequencies

at the  $\sigma_3$ -locations where Modes 1 and 2 cross at  $\beta_3=0.5$  are  $f^*=4561$  Hz and  $f^*=4291$  Hz for Mode 1 and 2, respectively. Even though the growth rates are similar at this wave number, the difference in the frequency is considered too large to suspect a multiple root there.

In Figures 4.4 - 4.6, the eigenfunctions of the two crossing Modes 1 and 3 of Figure 4.1 are plotted at three wave numbers at and near the point of their crossover. It is seen that the shape-functions of all disturbance quantities are very similar close to the crossover location at  $\beta_3=0.15$ . Further, the development of the shape-functions of both modes with an increasing wave number tangential to the constant phase lines indicates that the two modes indeed coincide. Hence, the existence of a multiple eigenvalue at  $x_1/c=0.6$  can be concluded.

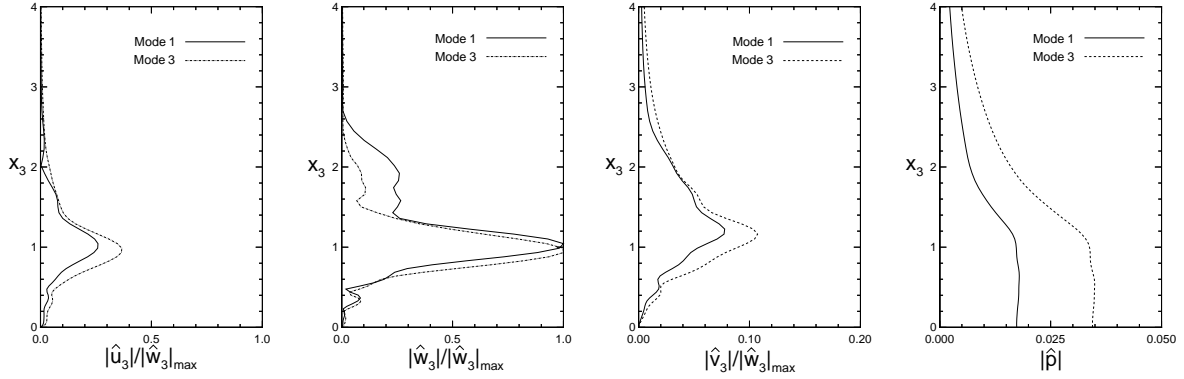


FIG. 4.4. Total shape-functions near the multiple eigenvalue at  $x_1/c=0.6$  ( $\beta_3=0.125$ )

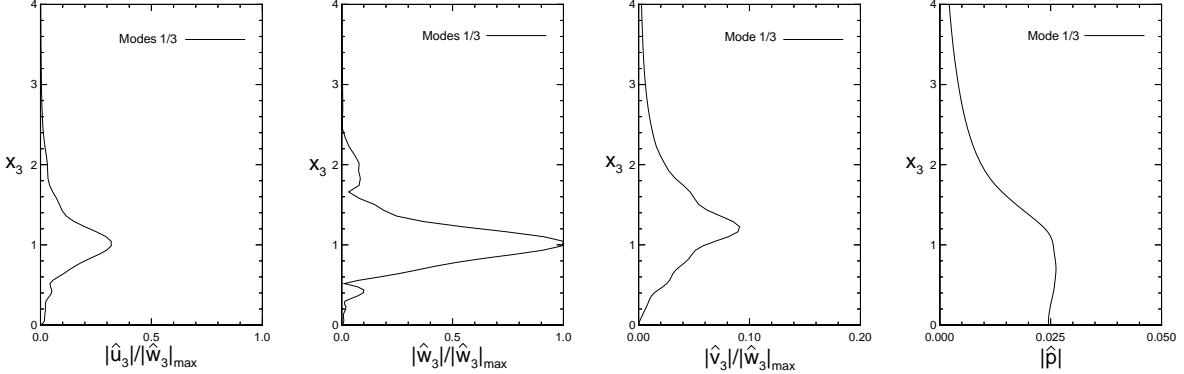


FIG. 4.5. Total shape-functions near the multiple eigenvalue at  $x_1/c=0.6$  ( $\beta_3=0.150$ )

Concluding the secondary instability analysis of the DLR Transition experiment, the structure of the secondary instability is examined. Considering the mode with the highest frequency at  $x_1/c=0.60$  (Mode 1), Figure 4.7 shows contours of the amplitude of the secondary eigenfunction tangential to the constant phase lines  $|w_3|$  for the most amplified wave number  $\beta_3=0.35$ , and iso-lines of the modified mean flow component in that direction in the Galilean coordinate system.

Superimposing the secondary structure on a modified mean flow component  $W_2$  that is assumed to be constant in the  $\bar{x}_1$ -direction, the total flow component tangential to the constant phase lines  $W_3 = W_2 + w_3$

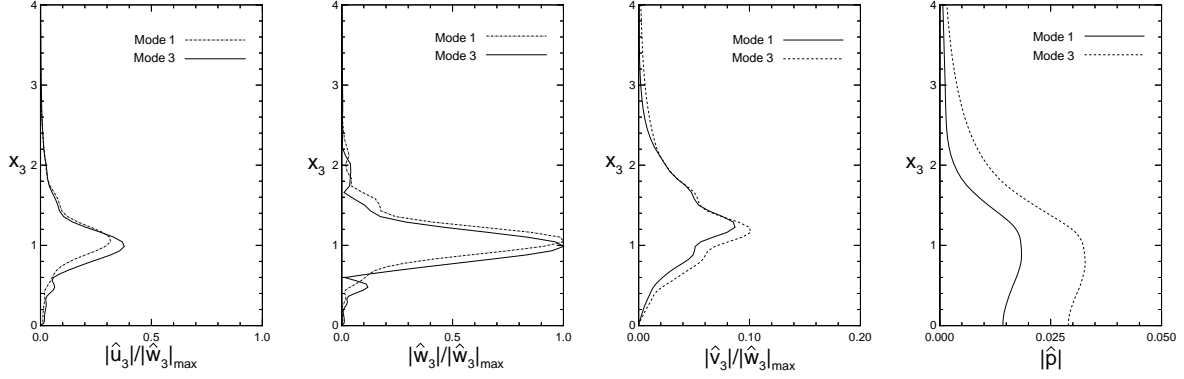


FIG. 4.6. Total shape-functions near the multiple eigenvalue at  $x_1/c=0.6$  ( $\beta_3=0.190$ )

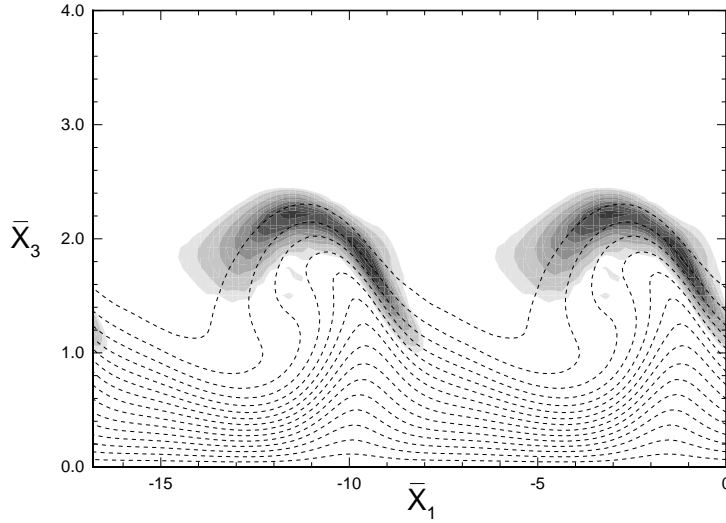


FIG. 4.7. Contours of  $|w_3|$  and  $W_2$  at  $x_1/c=0.6$  (axis in mm)

is obtained. Shown in Figure 4.9 is a top view of  $W_3$  contours at the same wall-normal location of  $\bar{x}_3=2.2$  as in Figure 4.8, where the secondary structure is assigned an amplitude of 1%. The dark patches correspond to lower-speed fluid traveling on the crest of the primary crossflow vortices in the  $\bar{x}_2$ -direction. The phase speed of these secondary disturbances  $C_{phase} = |\sigma_{3,imag}|/\beta_3 \cdot U_{e,0}^*/U_\infty^*$  is  $C_{phase} \simeq 1$ . Depending on their assigned amplitude, these secondary structures can severely modify the ordered primary structure of the stationary crossflow vortex.

From the observations in Figures 4.7 - 4.9, it seems that the structure of a single-frequency secondary instability is well defined and might be detected in experiments, if care is taken as to where the measurements are performed in the boundary layer.

**5. Conclusion.** In the second part of the present paper, we studied the secondary instability originating from a three-dimensional mean flow that is modified by the presence of purely stationary disturbances. Starting from equilibrium solutions that were obtained from nonlinear PSE computations, we used Floquet

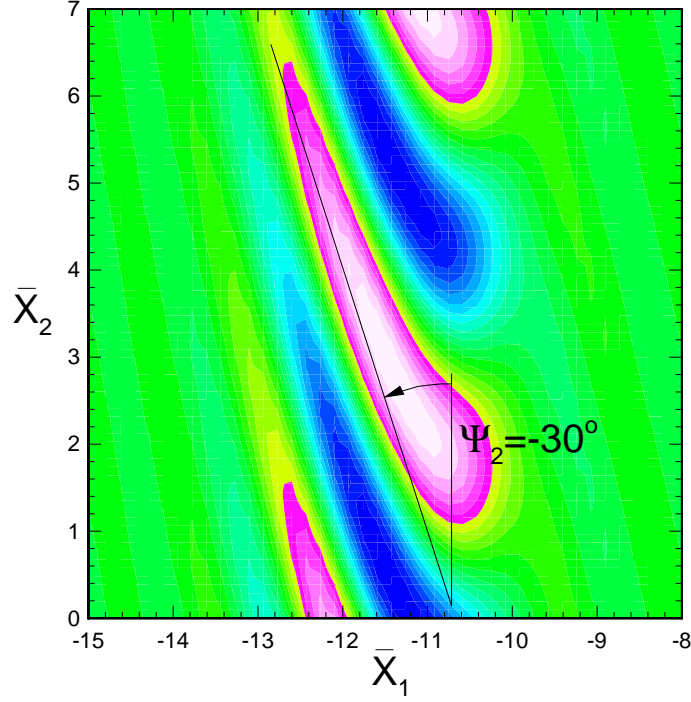


FIG. 4.8. Contours of  $w_3$  at  $x_1/c=0.6$  and  $\bar{x}_3=2.2\text{mm}$  ( $\alpha_3=-0.201$ ,  $\beta_3=0.35$ )

theory and developed global and local solvers that are based on the Implicitly Restarted Arnoldi Method and a Newton-Raphson technique, respectively.

For both the Swept Hiemenz Flow problem and the DLR Transition Experiment, several unstable eigenvalues were detected in the considered region of nonlinear amplitude saturation. The frequency of these traveling secondary disturbances is an order-of-magnitude higher than for the most amplified traveling primary disturbances. In contrast to the Swept Hiemenz Flow problem, where the few detected unstable and isolated eigenvalues indicate the dominance of a convective instability type in the transition process, the existence of a multiple eigenvalue was documented for the DLR Experiment at a chordwise location of  $x_1/c=0.60$ . The observation of this locally algebraic instability in an otherwise convectively unstable flow might explain the experimentally observed phenomena of a time dependent explosive growth of traveling disturbances.

For Swept Hiemenz Flow, the existence of a link between the unstable secondary eigenvalues and both the eigenvalue spectrum of the undisturbed mean flow and the continuous spectrum was established. It is concluded that there are at least three different mechanisms in the region of nonlinear saturation that cause high-frequency secondary instabilities. First, due to the action of the growing nonlinear disturbances, stable linear eigenmodes of the undisturbed mean flow are modified such that they develop into unstable secondary eigenmodes. Second, an inviscid high-frequency instability originates from the highly inflectional character of the modified mean flow profiles. Third, due to a not yet investigated receptivity mechanism, high-frequency disturbances from the continuous spectrum present in the outer flow enter the strongly distorted boundary

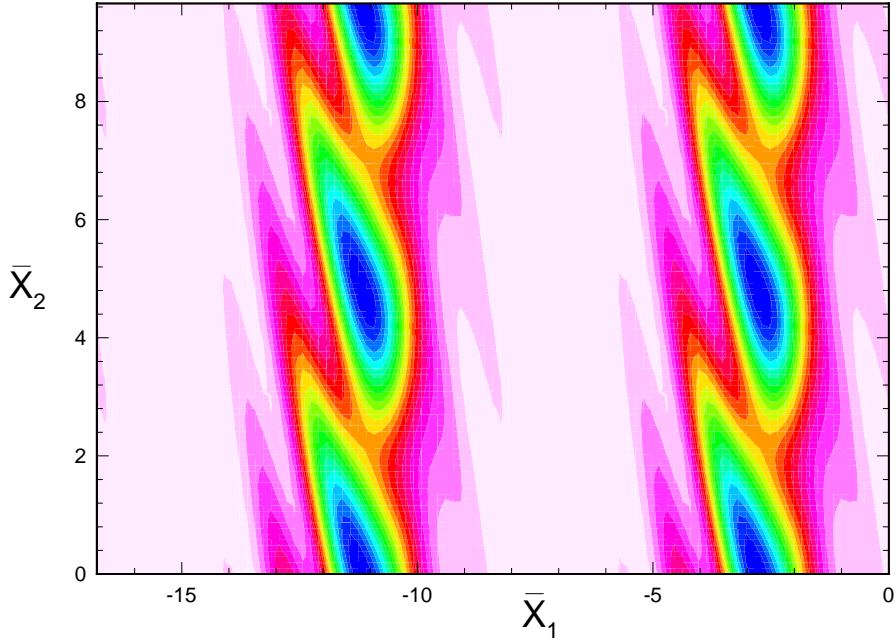


FIG. 4.9. Contours of  $W_3$  at  $x_1/c=0.6$  and  $\bar{x}_3=2.2\text{mm}$

layer in the region of nonlinear amplitude saturation. This corresponds to observations by Choudhari et al. [3], where they allocated the receptivity mechanism to regions of a strong variation in the boundary layer thickness. However, it is understood that the second mechanism represents the prevailing path to the transition in a crossflow instability dominated boundary layer.

Further considering Swept Hiemenz Flow, an unstable secondary mode at  $Re=546$  was traced back to its critical point by gradually decreasing the Reynolds number. The onset of this secondary instability was found at  $Re \simeq 475$  in a region where the primary stationary disturbances are about to saturate. The amplitudes of both the  $u_1$ - and  $w_1$ -disturbance components of the stationary crossflow vortex at this Reynolds number are  $\hat{A}_s = 11\%$ . This value agrees well with the prediction of the threshold amplitudes necessary for a self-sustained growth of the secondary disturbances of Mode 4 as obtained by artificially decreasing the primary disturbance amplitudes at  $Re=546$  ( $\hat{A}_s = 13\%$ ). Other detected eigenvalues at  $Re=546$  become unstable at threshold amplitudes of the primary disturbances as low as  $\hat{A}_s=5\%$  (Mode 3). Hence, secondary instabilities with small growth rates can be assumed to be present in a crossflow instability dominated flow even before the primary disturbances start to saturate. The impact of these weak secondary instabilities on the overall transition process, however, needs further investigation.

For both investigated flows, the obtained wave angles of the most unstable secondary disturbances closely correspond to previous work ([1], [13]). The most amplified secondary structures are inclined at angles between  $\Psi_2=-30^\circ$  and  $\Psi_2=-55^\circ$  with respect to the direction of the constant phase lines. Future work related to the research presented in Parts 1 and 2 will particularly focus on modeling the secondary instability more straightforwardly using the nonlinear PSE.

**Acknowledgments.** The authors wish to acknowledge the helpful cooperation with Dr. Bippes and Dr. Bertolotti from the DLR in Göttingen/Germany, who kindly provided the measured pressure distribution used in the computations of Section four. Also, we would like to express our appreciation of the provided generous access to the cluster of SUN workstations at ICASE, NASA Langley Research Center, in Hampton, Virginia.

## REFERENCES

- [1] S. BALACHANDAR, C.L. STREETT, AND M.R. MALIK, *Secondary instability in rotating-disc flow*, Journal of Fluid Mechanics **242** (1992), pp. 323–347.
- [2] P. BALAKUMAR AND M.R. MALIK, *Discrete modes and continuous spectra in supersonic boundary layers*, Journal of Fluid Mechanics **239** (1992), pp. 631–656.
- [3] M. CHOUDHARI, L. NG, AND C.L. STREETT, *A general approach for the prediction of localized instability generation in boundary layer flows*, Proc. R.A.S. Boundary Layer Transition and Control, Cambridge, U.K. (1991), pp. 45.1–45.20.
- [4] H. DEYHLE AND H. BIPPES, *Disturbance growth in an unstable three-dimensional boundary layer and its dependence on environmental conditions*, Journal of Fluid Mechanics **316** (1992), pp. 73–113.
- [5] T.M. FISCHER AND U. DALLMANN, *Primary and secondary instability analysis of a three-dimensional boundary layer flow*, Physics of Fluids A3 **10** (1991), pp. 2378–2391.
- [6] T.M. FISCHER, S. HEIN, AND U. DALLMANN, *A theoretical approach for describing secondary instability features in three-dimensional boundary layer flows*, AIAA Paper 93-0080, 1993.
- [7] TH. HERBERT, *Secondary Instability of plane channel flow to subharmonic 3D-disturbances*, Physics of Fluids **26**, No. 4 (1983), pp. 871–874.
- [8] W. KOCH, *On a degeneracy of temporal secondary instability modes in Blasius boundary layer flow*, Journal of Fluid Mechanics **243** (1992), pp. 319–351.
- [9] Y. KOHAMA, W.S. SARIC, AND J. HOOS, *A high-frequency secondary instability of crossflow vortices that leads to transition*, Proc. R.A.S. Boundary Layer Transition and Control, Cambridge U.K. (1991).
- [10] Y. KOHAMA, T. ONODERA, AND Y. EGAMI, *Design and control of crossflow instability field*, IUTAM Symposium on Nonlinear Instability and Transition in 3D Boundary Layers, Kluwer Academic Publishers, printed in the Netherlands, 1996, pp. 147–156.
- [11] R.B. LEHOUCQ, D.C. SORESENSEN, AND C. YANG, *ARPACK Users Guide*, to be obtained by <ftp://ftp.caam.rice.edu/pub/software/ARPACK>, 1997.
- [12] M.R. MALIK, S. CHUANG, AND M.Y. HUSSAINI, *Accurate numerical solution of compressible, linear stability equations*, Zeitschrift für Angewandte Mathematik und Physik **33**, No. 2 (1982), pp. 189–201.
- [13] M.R. MALIK, F. LI, AND C.-L. CHANG, *Crossflow disturbances in three-dimensional boundary layers: Nonlinear development, wave interaction and secondary instability*, Journal of Fluid Mechanics **268** (1994), pp. 1–36.
- [14] H.L. REED, *Wave interactions in swept wing flows*, Physics of Fluids **30** (1987), pp. 3419–3426.
- [15] W.S. SARIC AND L.G. YEATES, *Experiments on the stability of crossflow vortices in swept wing flows*, AIAA Paper 85-0493, 1985.
- [16] S.A. ORSZAG AND A.T. PATERA, *Secondary instability of wall-bounded shear flows*, Journal of Fluid Mechanics **128** (1993), pp. 347–385.
- [17] D.I.A. POLL, *Some observations of the transition process on the windward face of long yawed cylinder*,

- Journal of Fluid Mechanics **150** (1985), pp. 329–356.
- [18] S. TAKAGI AND N. ITOH, *Observation of traveling waves in the 3D-boundary layer along a yawed cylinder*, Fluid Dynamics Research **14** (1994), pp. 167–189.
- [19] T. WINTERGERSTE AND L. KLEISER, *DNS of transition in a three-dimensional boundary layer*, Transitional Boundary Layers in Aeronautics, North-Holland, Amsterdam, Oxford, New York, Tokyo (1996), pp. 145–153.